THE JOURNAL OF PHYSICAL CHEMISTRY LETTERS
A JOURNAL OF THE AMERICAN CHEMICAL SOCIETY

pubs.acs.org/JPCL

Letter

Monolayer Iridium Sulfide Halides with High Mobility Transport Anisotropy and Highly Efficient Light Harvesting

Yang Song, Jinbo Pan,* Yan-Fang Zhang, Haitao Yang, and Shixuan Du*

Cite This: *J. Phys. Chem. Lett.* 2021, 12, 6007−6013

Read Online

ACCESS | Metrics & More | Article Recommendations | Supporting Information

ABSTRACT: The discovery and design of two-dimensional semiconductors with high carrier mobilities is of vital importance for high-speed electronic and optoelectronic devices. Herein, based on high-throughput computations, we identify a group of semiconductors, iridium sulfide halides IrSX′ (X′ = F, Cl, Br, I), with high carrier mobilities (~10^3 cm^2 V^{-1} s^{-1}) and highly efficient light harvesting (~34%). Moreover, these materials exhibit anisotropic in-plane transport behavior, which is switchable via ferroelastic switching, providing the monolayer (ML) IrSX′s great potential for applications in direction-controlled high-speed electronic and optoelectronic devices. The high carrier mobility and anisotropic transport are stemming from the anisotropic distribution of 3d orbitals of Ir atoms at the conduction band minimum (CBM) and valence band maximum (VBM) in the rectangular lattices. The ML IrSX′s (X′ = F, Cl, Br) show good dynamical and thermal stabilities and are thermodynamically stable based on phase diagram calculations, thus meriting experimental realization in the future.

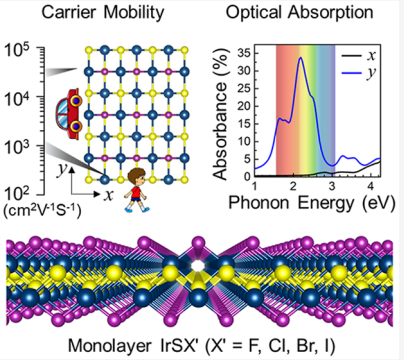

Two-dimensional (2D) materials are a class of nanostructured low-dimensional materials with great potential in fabricating the next generation of miniaturized electronic and optoelectronic devices.[1,2] The first 2D material, graphene, was successful fabricated in 2004[3,4] and has attracted considerable attention for its outstanding electronic characteristics, especially high carrier mobility, which is crucial in high-speed logic and radiofrequency devices.[3−6] However, a lack of a band gap in graphene hinders its wide applications in electronic logic circuits and optoelectronic devices. Great efforts have been devoted to tune the electronic properties of graphene; however, this has generated a serious deterioration of carrier mobilities with only a small band gap opening.[7−11] The discovery and design of other 2D semiconductors with sizable band gaps and high carrier mobilities are thus highly desirable.

In 2011, a monolayer (ML) MoS_2 field-effect transistor (FET) was fabricated, exhibiting high on/off current ratios and excellent current saturation characteristics but low carrier mobilities (<200 cm^2 V^{-1} s^{-1}).[12,13] Black phosphorus (α-P) exhibits relatively higher carrier mobilities; however, they are still orders of magnitude lower than that of graphene.[14,15] In addition, other artificially designed 2D materials were predicted to be semiconductors with high carrier mobilities.[16−22] However, the thermodynamic stability analysis is absent in most cases. Many hypothetical materials with exotic properties turn out to be unstable and impossible to synthesize.[23] Hence, the discovery and design of 2D semiconductors with high carrier mobilities and high thermodynamic stability are worthwhile and will provide potential candidates for future miniaturized electronic and optoelectronic devices.

In this work, we propose a feasible approach to screening promising 2D semiconductors with high carrier mobilities and high thermodynamic stabilities. A total of 45 semiconductors have been identified out of over 340 MXX′ (M = Sc, Ti, V, Cr, Mn, Fe, Co, Ni, Cu, Zn, Y, Zr, Nb, Mo, Tc, Ru, Rh, Pd, Ag, Cd, Hf, Ta, W, Re, Os, Ir, Pt, Au; X = S, Se, Te; X′ = F, Cl, Br, I) compounds, which were obtained by atom substitution of a prototype structure CrSBr.[24] As compared to binary materials with a specific prototype, there are more materials and more chances to discover excellent physical properties in these ternary families. In addition, there are two anions and one cation in the MXX′ family. It is easier to obtain clean band structures around the Fermi energy and semiconducting properties in this MXX′ family as compared to for those ternary compounds with two cations. Among them, the ML IrSX′ (X′ = F, Cl, Br, I) family is the most attractive candidate, which harbors a small absolute effective mass at the conduction band minimum (CBM) and valence band maximum (VBM) and high thermodynamic stabilities. Phonon-limited mobility calculations demonstrate that ML IrSX′ compounds possess high carrier mobilities and anisotropic transport along different

Received: April 6, 2021
Accepted: June 3, 2021
Published: June 24, 2021

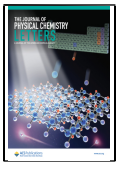

https://doi.org/10.1021/acs.jpclett.1c01086
J. Phys. Chem. Lett. 2021, 12, 6007−6013

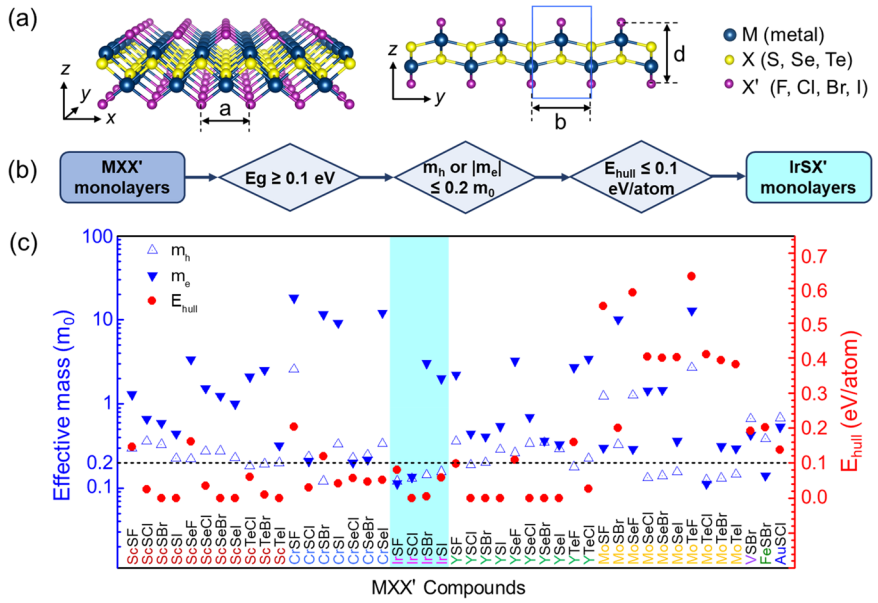

Figure 1. Atomic structure of ML MXX′s and materials discovery workflow. (a) Perspective view and side view of the atomic structure of ML MXX′s. (b) Flowchart for picking out ML IrSX′s from ML MXX′s. (c) Minimum hole (m_h) and electron (m_e) effective masses of ML MXX′s and energy above convex hull (E_{hull}) of bulk MXX′s.

directions. ML IrSF is the most prominent material exhibiting ultrahigh hole mobility. Furthermore, ML IrSF exhibits strong light absorbance up to 34% in the visible-light range along the *y* direction, much larger than that of the black phosphorus. The formation enthalpies of IrSF, IrSCl, and IrSBr are all on the convex hull in the Ir−S−X′ ternary phase diagrams, while that of IrSI is close to the convex hull in the phase diagram.[25] These results indicate a great potential for the IrSX′ family to be synthesized, and experimental realization is thus called for.

The crystal structure of ML MXX′ shown in Figure 1a has a *Pmmn* (C_{2v}) space group. The buckled MX layer is sandwiched between two halogen layers by M−X′ bonds. Each metal (M) atom is six-coordinated with four chalcogen (X = S, Se, Te) atoms and two halogen (X′ = F, Cl, Br, I) atoms. The primitive cell, containing two M, two X, and two X′ atoms, is marked by a blue rectangle in the side view of the atomic structure in Figure 1a. In the screening process (Figure 1b), three criteria at the initial steps are considered, including the band gap, effective mass, and energy above convex hull,[25] respectively.

At the first step, we pick out 45 ML MXX′ semiconductors with band gaps larger than 0.1 eV at the PBE level from over 340 MXX′ compounds as shown in Figure 1c. Most of the semiconductors are distributed in three subfamilies, namely, the $M_{IIIB}XX'$ (M_{IIIB} = Sc, Y), $M_{VIB}XX'$ (M_{VIB} = Cr, Mo), and IrXX′ subfamilies, respectively.

Since effective mass (m^*) is inversely related to carrier mobilities,[14,26] we then use it as a screening criterion to look for materials with high mobilities and to keep a balance between efficiency and accuracy of materials prediction. Considering the effective masses have positive and negative values, here we only present the smallest absolute value for each material in Figure 1c. We find that the hole effective masses of most MXX′ compounds are smaller than electron effective masses, especially for the ScXX′ and YXX′ compounds. While IrSF, IrSCl, MoTeCl, and several Cr-related compounds have similar hole and electron effective masses. The effective mass is closely related to the orbitals contributing to the CBM and VBM, which has been discussed in the previous literature.[27] Here, we use $m^* < 0.2\ m_0$ as a criterion to screen the potential materials. After this step, 45 ML semiconductors with either hole or electron effective masses smaller than 0.2 m_0 have been selected, including ScTeCl, CrSBr, IrSX′, YSCl, YTeF, MoXX′ (X = Se, Te; X′ = Cl, Br, I), and FeSBr.

The formation enthalpies of ML MXX′ are used to calculate the energy above the convex hull. Detailed information can be found in the *Calculation Methods* section in the Supporting Information. Although this method underestimates the thermodynamic stabilities of MXX′ compounds due to the absence of the interlayer interactions in the MLs, the uncertainty values are usually tens of meV/Å^2,[28] which will not affect the qualitative results. We use $E_{hull} < 0.1$ eV/atom as the criterion to screen the most potentially synthesizable materials. The materials in IrSX′ family, highlighted by cyan, satisfy the low-E_{hull} criterion and thus are selected as the most promising candidates.

The geometric information on ML IrSX′s is summarized in Table S1. The phonon dispersions of the ML IrSX′s are calculated to evaluate the dynamical stability, as depicted in Figure S1. No imaginary frequency is observed in their phonon spectra, indicating that ML IrSX′s are dynamically stable. The ab initio molecular dynamic (AIMD) simulations are carried out to evaluate the thermostabilities of ML IrSX′s (Figure S2). The structural integrity after the AIMD simulations prove that the ML IrSX′s are all stable at room temperature.

The band structures of ML IrSX′s at the PBE level are presented in Figure S3. ML IrSF is a direct band gap semiconductor with a band gap of 0.38 eV. While ML IrSCl, IrSBr, and IrSI are indirect band gap semiconductors with band gaps of 0.30, 0.30, and 0.20 eV, respectively, their direct band gaps are only slightly larger than the indirect band gaps. Because the hybrid functional usually provides more reliable electronic structures for traditional semiconductors, in Figure 2, we show the band structures of ML IrSX′s obtained by the HSE06 functional. The differences between their indirect band gaps and direct band gaps are very small, especially for IrSF,

https://doi.org/10.1021/acs.jpclett.1c01086
J. Phys. Chem. Lett. 2021, 12, 6007−6013

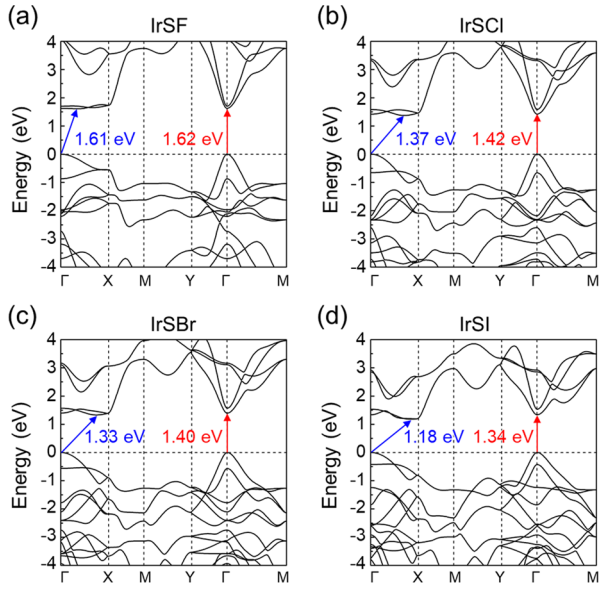

Figure 2. Band structures of ML IrSX′s calculated with the HSE06 functional. The blue arrows mark the band gaps. The red arrows mark the direct band gaps at the Γ point. The band gap decreases from IrSF to IrSI.

IrSCl, and IrSBr, and thus can be regarded as direct band gap semiconductors. All the band structures of ML IrSX′ show large anisotropic dispersion close to Fermi energy. The dispersion around VBMs and CBMs is relatively flat along the Γ−X direction while very sharp along the Γ−Y direction for these four IrSX′ materials. This phenomenon suggests that the absolute value of carrier effective mass along the Γ−Y direction will be much smaller than that along the Γ−X direction, indicating a possibly anisotropic transport of IrSX′ compounds along different directions.

We then calculate the carrier mobilities of ML IrSX′s. Based on the deformation potential theory,[29,30] the acoustic phonon-limited carrier mobility can be estimated by the following formula[14,26]

$$\mu_{2D} = \frac{e\hbar^3 C_{2D}}{k_B T m_e^* m_d E_d^2}$$

where e, $\hbar$, k_B, and T are the electron charge, Planck constant, Boltzmann constant, and temperature, respectively. m^* is the effective mass in the transport direction, and m_d is the average effective mass defined as $m_d = \sqrt{m_x^* m_y^*}$. C_{2D} is the elastic modulus, and E_d is the deformation potential. More detailed information about the calculation methods can be found in the *Calculation Methods* section in the Supporting Information.

Table 1. In-Plane Elastic Moduli (C_{2D}), Effective Masses (m^*), Deformation Potentials (E_d), and Carrier Mobilities (μ) of ML IrSX′s

	carrier type	direction	C_{2D} (J m^{-2})	m^* (m_0)	E_d (eV)	μ (cm^2 V^{-1} s^{-1})
IrSF (PBE)	electron	x	130.20	11.57	2.52	32.99
		y	178.74	0.11	6.28	743.10
	hole	x	130.20	2.23	1.27	1472.45
		y	178.74	0.12	1.68	21 401.33
IrSF (PBE + SOC)	electron	x	128.27	22.39	2.16	15.73
		y	169.74	0.12	6.53	411.78
	hole	x	128.27	2.33	1.49	948.05
		y	169.74	0.13	1.39	25 758.67
IrSF (HSE06)	electron	x	147.46	3.98	3.45	94.09
		y	219.39	0.13	9.38	601.80
	hole	x	147.46	2.35	1.63	887.42
		y	219.39	0.14	3.27	5687.26
IrSCl (PBE)	electron	x	112.27	2.63	2.07	364.35
		y	170.34	0.13	7.26	906.89
	hole	x	112.27	1.63	1.29	1873.44
		y	170.34	0.13	1.88	16 195.08
IrSBr (PBE)	electron	x	102.44	1.68	2.39	472.10
		y	169.60	0.14	7.47	959.72
	hole	x	102.44	1.75	2.00	621.13
		y	169.60	0.14	2.35	9177.25
IrSI (PBE)	electron	x	97.26	0.97	2.34	973.60
		y	165.62	0.16	7.61	928.51
	hole	x	97.26	1.94	2.35	352.72
		y	165.62	0.16	3.13	4182.54
BP (PBE)	electron	x	21.50	0.17	0.71	11 361.29
		y	91.43	1.24	4.20	191.52
	hole	x	21.50	0.16	2.74	341.30
		y	91.43	7.64	1.92	62.63
BP (HSE06)	electron	x	27.28	0.19	0.87	8547.60
		y	106.29	1.10	4.69	202.90
	hole	x	27.28	0.17	3.13	381.76
		y	106.29	4.64	1.82	164.15

https://doi.org/10.1021/acs.jpclett.1c01086
J. Phys. Chem. Lett. 2021, 12, 6007−6013

The calculated carrier mobilities under room temperature and other parameters of ML IrSX′s are listed in Table 1. As a benchmark, the carrier mobilities of ML black phosphorus are also studied for comparison. All the ML IrSX′s have larger hole mobilities than electron mobilities. The mobilities along the y direction are also larger than those along the x direction except for IrSI. In particular, IrSF has the largest hole mobility, while all the four ML IrSX′s have comparable electron mobilities. Interestingly, the PBE calculation results demonstrate that the hole mobility in the dominant transport direction of IrSF is even larger than that of ML black phosphorus. Meanwhile, the hole mobility obtained by HSE06 calculations is comparable with that of ML black phosphorus obtained using the same functional, suggesting its potential for high-performance electronic applications. Our calculated carrier mobilities of ML black phosphorus also match well with those in previous literature using the same HSE06 functional.[31] Since the Ir element is heavy, taking IrSF as an example, we also calculate its carrier mobilities considering the spin−orbital coupling (SOC) effect, as is also shown in Table 1. Except for the electron effective mass along the x direction, all the other parameters slightly change. Its carrier mobilities with and without the SOC effect are in the same order.

Next, we choose the most outstanding material IrSF to analyze the mechanisms of the ultrahigh carrier mobilities and anisotropic transport properties using the HSE06 results. μ_{2D} is proportional to the elastic modulus C_{2D} and is inversely proportional to the effective mass m^* and the square of deformation potential E_d^2. By comparing the parameters along the x direction and those along the y direction (Table 1), we find that the small effective mass m^* is the main factor resulting in the high carrier mobilities along the y direction. The effective carrier masses along the Γ−Y direction are rather small, 0.14 m_0 for holes and 0.13 m_0 for electrons, whereas these along Γ−X are much larger, 2.35 m_0 for holes and 3.98 m_0 for electrons. Also, the elastic modulus C_{2D} is another factor that effectively influences the carrier mobility. Except for IrSI, all the other IrSX′ materials have a larger C_{2D} along the y direction, further enhancing the transport anisotropy along the x and y directions. The deformation potentials E_d, which are the same order of magnitude as typical values of E_d, such as graphene (5.0 eV),[30] MoS_2 (3.9 eV),[32] h-BN (3.7 eV),[33] and AlGaAs quantum wells (7 eV),[34] are thus not a key term in causing high mobilities of ML IrSX′s.

As demonstrated in the previous literature, the anisotropic transport is not only a geometric effect but also has close relation to the electronic structures.[21,22] Since the effective masses and elastic moduli are all related to electronic properties, we then turn to study the electronic properties of IrSF. As can be seen in the projected density of states (PDOS) of IrSF in Figure 3a,b, the VBM and CBM are both dominated by 3d orbitals of Ir atoms. The VBM is mainly dominated by the Ir-d_{yz} orbital, while the CBM is mainly dominated by Ir-d_{z^2} and Ir-$d_{x^2-y^2}$ orbitals. The partial charge density distributions at the VBM and CBM are shown in Figure 3c,d. Since the orbital lobes at both the VBM and CBM are along the y direction, there is much more charge density between Ir and S atoms along the y direction than those along the x direction, leading to a larger band dispersion and elastic modulus along the y direction. The intrinsic electronic structures and mechanical properties of IrSX′ are closely correlated to their buckled geometric structures. Along the x direction, two neighboring Ir atoms are mediated by one S atom and one X′ atom. Because

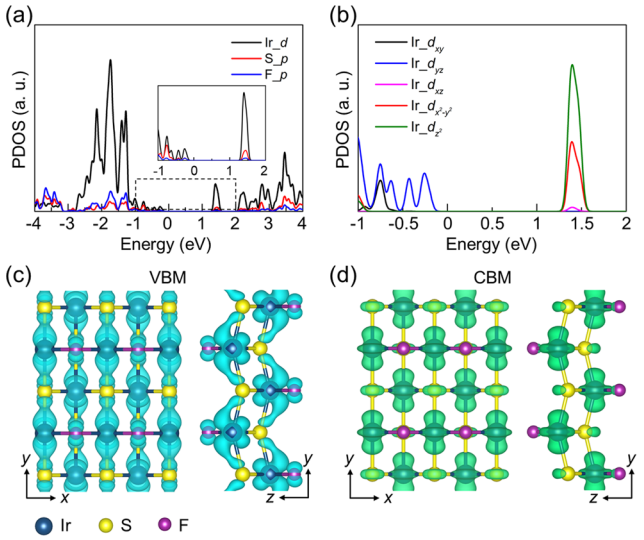

Figure 3. Electronic properties of ML IrSF. (a) PDOS of ML IrSF on different atoms and orbitals. (b) PDOS of Ir atoms on d orbitals. (c,d) Charge density at the VBM and CBM. The isosurface values are 0.01 e/Bohr^3.

the atomic radius of the halide atom is smaller than that of the S atom, the Ir−S−Ir angle is modulated by the choice of halide atom, and a large Ir−S−Ir angle occurs in this direction. Along the y direction, due to the absence of such Ir−X′ bonds, the Ir−S−Ir angle is close to straight angle. In this case, the p orbital of the S atom has more of a chance to overlap with the neighboring Ir atoms, leading to much delocalized orbitals and thus a smaller effective mass along the y direction; it can also explain why these four IrSX′ compounds have the same lattice constants along y direction as shown in Table S1. It is easy to understand that the larger Ir−S−Ir angle corresponds to a large elastic modulus; the C_{2D} along the y direction is thus larger.

The significant anisotropic carrier mobilities are closely related to the anisotropic geometric structures. External strain could possibly tune the geometric structure and thus electronic properties. We therefore explore the strain effect on the ML IrSF. Interestingly, the ML IrSF is found to be ferroelastic material. The computed transition path and the transition energy barrier using the ss-NEB method are shown in Figure S4. The calculated ferroelastic switching barrier is 0.31 eV per atom, which is comparable with those of phosphorene (0.20 eV per atom),[35] 2H VSSe (0.23 eV per atom),[36] and BP_5 (0.32 eV per atom).[37] Therefore, it is possible to achieve the precise direction control of the carrier migration via ferroelastic switching.

The deformation potential theory has been widely used to predict intrinsic mobilities of materials; it can only give an approximate result for carrier mobility. More accurate but more expensive calculations considering the electron−phonon coupling effect are also employed to estimate the mobilities of monolayer IrSF. The calculation details can be found in the *Calculation Methods* section. The hole (electron) mobility in monolayer IrSF, computed for a carrier concentration of 1×10^{18} cm^{-2} at 300 K along the dominant transport direction and the perpendicular direction, is 4300 cm^2 V^{-1} s^{-1} (2600 cm^2 V^{-1} s^{-1}) and 82 cm^2 V^{-1} s^{-1} (27 cm^2 V^{-1} s^{-1}), respectively. The high hole mobility and anisotropic property are similar to those calculated using deformation potential theory. We found

https://doi.org/10.1021/acs.jpclett.1c01086
J. Phys. Chem. Lett. 2021, 12, 6007−6013

that the electron mobility is almost independent of carrier concentration ranging from 10^{15} to 10^{19} cm^{-2}.

The HSE06 band gaps of IrSX′s vary from 1.2 to 1.6 eV, suggesting possibly high optical absorption in the visible-light range. The optical absorption spectra of ML IrSF are shown in Figure 4. Strong light absorbance in the visible-light range

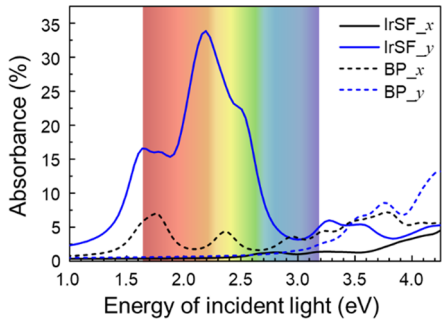

Figure 4. Optical absorption spectra of ML IrSF (solid lines) and ML black phosphorus (dash lines) for light incident in the z direction and polarized along the x (black lines) and y (blue lines) directions, respectively.

(1.64−3.19 eV) along the y direction, up to 34%, is observed. Meanwhile, the visible-light absorbance along the x direction is found to be extremely low, less than 2%. Therefore, ML IrSF strongly absorbs y-polarized visible light and is transparent to x-polarized visible light. This anisotropic optical property is caused by the in-plane anisotropy of the structure and makes ML IrSF to be an intrinsic optical linear polarizer and a polarization-sensitive photodetector. We also calculate the optical absorption spectra of ML black phosphorus for comparison. The visible-light absorbance of IrSF along the y direction is much larger than that of the anisotropic ML black phosphorus.

The ML IrSX′s show prominent carrier mobilities, excellent anisotropic transport, and light absorbance, and thus, the experimental fabrication possibility becomes a crucial issue. The exfoliation energy of IrSF is 37.0 meV/Å^2, which is smaller than the suggested potential exfoliable energy of ∼200 meV/Å^2.[28] Since the formation enthalpies of bulk materials are always lower than those of monolayers due to their interlayer interactions, we then investigate the thermodynamic stabilities of the IrSX′ bulk materials. To provide a useful guideline for future fabrication, we investigate the ternary phase diagrams of Ir−S−X′, as shown in Figure 5. The ternary phase diagrams are obtained by collection of the minimum formation enthalpies of materials with particular compositions. More calculation details can be found in the *Calculation Methods* section in the Supporting Information. As can be seen, the formation enthalpies of bulk IrSX′s except for IrSI are all on the convex hull, while that of IrSI is only 2.0 meV energy above the convex hull. These results indicate that IrSX′ compounds are all thermodynamically stable. The IrSX′ compounds are possibly prepared by mixing Ir_2S_3 and IrX'_3 compounds using chemical vapor deposition (CVD) or other methods; therein, synthesis of IrSCl should be the easiest, since it has almost the lowest formation enthalpy in the Ir−S−Cl ternary phase diagram.

By performing high-throughput computations based on density functional theory, we identify 45 2D semiconductors out of over 340 MXX′ compounds. The effective masses and energies above the convex hull are calculated, which reveal strong correlation to cation atoms. Among them, the ML IrSX′s have almost the lowest energies above the convex hulls and the smallest effective masses. Ultrahigh carrier mobilities (∼10^3 cm^2 V^{-1} s^{-1}) and anisotropic transports are revealed in ML IrSX′s. The high carrier mobility mainly results from the small effective mass at the VBM along the dominant transport direction, while the in-plane anisotropic transport stems from the anisotropic distribution of 3d orbitals of Ir atoms at the CBM and VBM in the rectangular lattices. Interestingly, ML

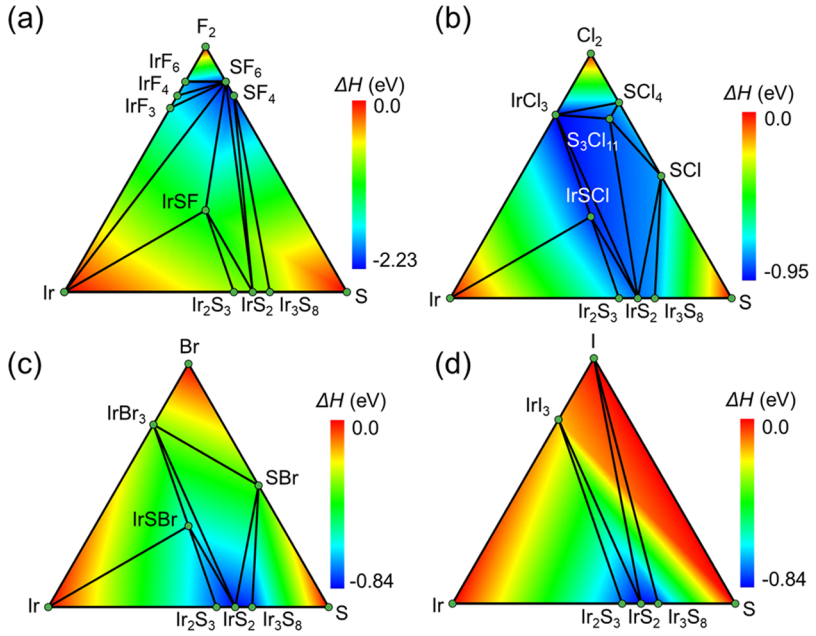

Figure 5. Ternary phase diagrams of bulk IrSX′s. Only the materials on the convex hull are shown in the phase diagrams. The formation enthalpies are labeled by color. Bulk (a) IrSF, (b) IrSCl, and (c) IrSBr are all on the energy convex hull, while bulk (d) IrSI is 2.0 meV/atom above the convex hull and is not shown.

https://doi.org/10.1021/acs.jpclett.1c01086
J. Phys. Chem. Lett. 2021, 12, 6007−6013

IrSX′s show ferroelasticity and the ferroelastic switching under external strain provides a flexible approach to control the direction-dependent carrier migration. Moreover, the optical absorption spectra of ML IrSF reveal highly efficient light harvesting (∼34%). This unique combination of excellent electronic, optoelectronic, and mechanical properties of the versatile IrSX′ compounds offers a great opportunity in future electronic and optoelectronic devices.

■ ASSOCIATED CONTENT

Supporting Information

The Supporting Information is available free of charge at https://pubs.acs.org/doi/10.1021/acs.jpclett.1c01086.

Calculation methods, the lattice constants, the AIMD simulation, and the band structures of ML IrSX′ at the PBE level; the ferroelastic switching of ML IrSF under stress (PDF)

■ AUTHOR INFORMATION

Corresponding Authors

Jinbo Pan − *Institute of Physics & University of Chinese Academy of Sciences, Chinese Academy of Sciences, Beijing 100190, China; Beijing National Laboratory for Condensed Matter Physics, Beijing 100190, China*; Email: jbpan@iphy.ac.cn

Shixuan Du − *Institute of Physics & University of Chinese Academy of Sciences, Chinese Academy of Sciences, Beijing 100190, China; Beijing National Laboratory for Condensed Matter Physics, Beijing 100190, China; CAS Center for Excellence in Topological Quantum Computation, Beijing 100190, China; Songshan Lake Materials Laboratory, Dongguan 523808, China*; orcid.org/0000-0001-9323-1307; Email: sxdu@iphy.ac.cn

Authors

Yang Song − *Institute of Physics & University of Chinese Academy of Sciences, Chinese Academy of Sciences, Beijing 100190, China; Beijing National Laboratory for Condensed Matter Physics, Beijing 100190, China*

Yan-Fang Zhang − *Institute of Physics & University of Chinese Academy of Sciences, Chinese Academy of Sciences, Beijing 100190, China*

Haitao Yang − *Institute of Physics & University of Chinese Academy of Sciences, Chinese Academy of Sciences, Beijing 100190, China*

Complete contact information is available at: https://pubs.acs.org/10.1021/acs.jpclett.1c01086

Notes

The authors declare no competing financial interest.

■ ACKNOWLEDGMENTS

This work was supported by grants from the National Natural Science Foundation of China (61888102), the National Key Research and Development Projects of China (2016YFA0202300), and the Strategic Priority Research Program of the Chinese Academy of Sciences (XDB30000000). Computational resources were provided by the National Supercomputing Center in Tianjin.

■ REFERENCES

(1) Wang, Q. H.; Kalantar-Zadeh, K.; Kis, A.; Coleman, J. N.; Strano, M. S. Electronics and Optoelectronics of Two-Dimensional Transition Metal Dichalcogenides. *Nat. Nanotechnol.* **2012**, *7*, 699−712.

(2) Song, J.; Xu, L.; Li, J.; Xue, J.; Dong, Y.; Li, X.; Zeng, H. Monolayer and Few-Layer All-Inorganic Perovskites as a New Family of Two-Dimensional Semiconductors for Printable Optoelectronic Devices. *Adv. Mater.* **2016**, *28*, 4861−4869.

(3) Novoselov, K. S.; Geim, A. K.; Morozov, S. V.; Jiang, D.; Zhang, Y.; Dubonos, S. V.; Grigorieva, I. V.; Firsov, A. A. Electric Field Effect in Atomically Thin Carbon Films. *Science* **2004**, *306*, 666.

(4) Berger, C.; Song, Z.; Li, T.; Li, X.; Ogbazghi, A. Y.; Feng, R.; Dai, Z.; Marchenkov, A. N.; Conrad, E. H.; First, P. N.; et al. Ultrathin Epitaxial Graphite: 2D Electron Gas Properties and a Route Toward Graphene-Based Nanoelectronics. *J. Phys. Chem. B* **2004**, *108*, 19912−19916.

(5) Novoselov, K. S.; Geim, A. K.; Morozov, S. V.; Jiang, D.; Katsnelson, M. I.; Grigorieva, I. V.; Dubonos, S. V.; Firsov, A. A. Two-Dimensional Gas of Massless Dirac Fermions in Graphene. *Nature* **2005**, *438*, 197−200.

(6) Hwang, E. H.; Adam, S.; Sarma, S. D. Carrier Transport in Two-Dimensional Graphene Layers. *Phys. Rev. Lett.* **2007**, *98*, 186806.

(7) Sofo, J. O.; Chaudhari, A. S.; Barber, G. D. Graphane: A Two-Dimensional Hydrocarbon. *Phys. Rev. B: Condens. Matter Mater. Phys.* **2007**, *75*, 153401.

(8) Elias, D. C.; Nair, R. R.; Mohiuddin, T. M. G.; Morozov, S. V.; Blake, P.; Halsall, M. P.; Ferrari, A. C.; Boukhvalov, D. W.; Katsnelson, M. I.; Geim, A. K.; et al. Control of Graphene's Properties by Reversible Hydrogenation: Evidence for Graphane. *Science* **2009**, *323*, 610.

(9) Samarakoon, D. K.; Wang, X.-Q. Chair and Twist-Boat Membranes in Hydrogenated Graphene. *ACS Nano* **2009**, *3*, 4017−4022.

(10) Son, Y.-W.; Cohen, M. L.; Louie, S. G. Half-Metallic Graphene Nanoribbons. *Nature* **2006**, *444*, 347−349.

(11) Li, X.; Wang, X.; Zhang, L.; Lee, S.; Dai, H. Chemically Derived, Ultrasmooth Graphene Nanoribbon Semiconductors. *Science* **2008**, *319*, 1229.

(12) Mak, K. F.; Lee, C.; Hone, J.; Shan, J.; Heinz, T. F. Atomically Thin MoS_2: A New Direct-Gap Semiconductor. *Phys. Rev. Lett.* **2010**, *105*, 136805.

(13) Radisavljevic, B.; Radenovic, A.; Brivio, J.; Giacometti, V.; Kis, A. Single-Layer MoS_2 Transistors. *Nat. Nanotechnol.* **2011**, *6*, 147−150.

(14) Fei, R.; Yang, L. Strain-Engineering the Anisotropic Electrical Conductance of Few-Layer Black Phosphorus. *Nano Lett.* **2014**, *14*, 2884−2889.

(15) Li, L.; Yu, Y.; Ye, G. J.; Ge, Q.; Ou, X.; Wu, H.; Feng, D.; Chen, X. H.; Zhang, Y. Black Phosphorus Field-Effect Transistors. *Nat. Nanotechnol.* **2014**, *9*, 372−377.

(16) Guo, Z.; Zhou, J.; Zhu, L.; Sun, Z. MXene: A Promising Photocatalyst for Water Splitting. *J. Mater. Chem. A* **2016**, *4*, 11446−11452.

(17) Zhang, S.; Xie, M.; Li, F.; Yan, Z.; Li, Y.; Kan, E.; Liu, W.; Chen, Z.; Zeng, H. Semiconducting Group 15 Monolayers: A Broad Range of Band Gaps and High Carrier Mobilities. *Angew. Chem., Int. Ed.* **2016**, *55*, 1666−1669.

(18) Zhang, T.; Ma, Y.; Yu, L.; Huang, B.; Dai, Y. Direction-Control of Anisotropic Electronic Behaviors via Ferroelasticity in Two-Dimensional α-MPI (M = Zr, Hf). *Mater. Horiz.* **2019**, *6*, 1930−1937.

(19) Tang, C.; Ma, F.; Zhang, C.; Jiao, Y.; Matta, S. K.; Ostrikov, K.; Du, A. 2D Boron Dichalcogenides from the Substitution of Mo with Ionic B_2 Pair in MoX_2 (X = S, Se and Te): High Stability, Large Excitonic Effect and High Charge Carrier Mobility. *J. Mater. Chem. C* **2019**, *7*, 1651−1658.

(20) Tang, C.; Zhang, L.; Zhang, C.; MacLeod, J.; Ostrikov, K.; Du, A. Highly Stable Two-Dimensional Gold Selenide with Large In-Plane

Anisotropy and Ultrahigh Carrier Mobility. *Nanoscale Horiz.* **2020**, *5*, 366−371.
(21) Yin, Y.; Shao, C.; Zhang, C.; Zhang, Z.; Zhang, X.; Robertson, J.; Guo, Y. Anisotropic Transport Property of Antimonene MOSFETs. *ACS Appl. Mater. Interfaces* **2020**, *12*, 22378−22386.
(22) Liao, Y.; Zhang, Z.; Gao, Z.; Qian, Q.; Hua, M. Tunable Properties of Novel Ga_2O_3 Monolayer for Electronic and Optoelectronic Applications. *ACS Appl. Mater. Interfaces* **2020**, *12*, 30659−30669.
(23) Zunger, A. Beware of Plausible Predictions of Fantasy Materials. *Nature* **2019**, *566*, 447−449.
(24) Göser, O.; Paul, W.; Kahle, H. G. Magnetic Properties of CrSBr. *J. Magn. Magn. Mater.* **1990**, *92*, 129−136.
(25) Barber, C. B.; Dobkin, D. P.; Huhdanpaa, H. The Quickhull Algorithm for Convex Hulls. *ACM Trans. Math. Softw.* **1996**, *22*, 469−483.
(26) Qiao, J.; Kong, X.; Hu, Z.-X.; Yang, F.; Ji, W. High-Mobility Transport Anisotropy and Linear Dichroism in Few-Layer Black Phosphorus. *Nat. Commun.* **2014**, *5*, 4475.
(27) Hautier, G.; Miglio, A.; Ceder, G.; Rignanese, G.-M.; Gonze, X. Identification and Design Principles of Low Hole Effective Mass P-Type Transparent Conducting Oxides. *Nat. Commun.* **2013**, *4*, 2292.
(28) Mounet, N.; Gibertini, M.; Schwaller, P.; Campi, D.; Merkys, A.; Marrazzo, A.; Sohier, T.; Castelli, I. E.; Cepellotti, A.; Pizzi, G.; et al. Two-Dimensional Materials from High-Throughput Computational Exfoliation of Experimentally Known Compounds. *Nat. Nanotechnol.* **2018**, *13*, 246−252.
(29) Wei, S.-H.; Zunger, A. Predicted Band-Gap Pressure Coefficients of All Diamond and Zinc-Blende Semiconductors: Chemical Trends. *Phys. Rev. B: Condens. Matter Mater. Phys.* **1999**, *60*, 5404−5411.
(30) Xi, J.; Long, M.; Tang, L.; Wang, D.; Shuai, Z. First-Principles Prediction of Charge Mobility in Carbon and Organic Nanomaterials. *Nanoscale* **2012**, *4*, 4348−4369.
(31) Sun, J.; Lin, N.; Ren, H.; Tang, C.; Yang, L.; Zhao, X. The Electronic Structure, Mechanical Flexibility and Carrier Mobility of Black Arsenic-Phosphorus Monolayers: A First Principles Study. *Phys. Chem. Chem. Phys.* **2016**, *18*, 9779−9787.
(32) Kaasbjerg, K.; Thygesen, K. S.; Jacobsen, K. W. Phonon-Limited Mobility in N-Type Single-Layer MoS_2 from First Principles. *Phys. Rev. B: Condens. Matter Mater. Phys.* **2012**, *85*, 115317.
(33) Bruzzone, S.; Fiori, G. Ab-Initio Simulations of Deformation Potentials and Electron Mobility in Chemically Modified Graphene and Two-Dimensional Hexagonal Boron-Nitride. *Appl. Phys. Lett.* **2011**, *99*, 222108.
(34) Walukiewicz, W.; Ruda, H. E.; Lagowski, J.; Gatos, H. C. Electron Mobility in Modulation-Doped Heterostructures. *Phys. Rev. B: Condens. Matter Mater. Phys.* **1984**, *30*, 4571−4582.
(35) Wu, M.; Zeng, X. C. Intrinsic Ferroelasticity and/or Multiferroicity in Two-Dimensional Phosphorene and Phosphorene Analogues. *Nano Lett.* **2016**, *16*, 3236−3241.
(36) Zhang, C.; Nie, Y.; Sanvito, S.; Du, A. First-Principles Prediction of a Room-Temperature Ferromagnetic Janus VSSe Monolayer with Piezoelectricity, Ferroelasticity, and Large Valley Polarization. *Nano Lett.* **2019**, *19*, 1366−1370.
(37) Wang, H.; Li, X.; Sun, J.; Liu, Z.; Yang, J. BP_5 Monolayer with Multiferroicity and Negative Poisson's Ratio: A Prediction by Global Optimization Method. *2D Mater.* **2017**, *4*, 045020.

https://doi.org/10.1021/acs.jpclett.1c01086
J. Phys. Chem. Lett. 2021, 12, 6007−6013